



Coherent nanointerface between light-harvesting and catalytic transition metal sulfides for efficient photochemical conversion

Yuexing Chen^{a,b,1}, Ming Ma^{c,1}, Jun Hu^{d,1}, Zhong Chen^e, Peng Jiang^f, Lilac Amirav^{b,*}, Shihe Yang^{g,*}, Zheng Xing^{a,*}

^a School of Chemical Engineering and Technology, Sun Yat-sen University, Zhuhai 519082, China

^b Schulich Faculty of Chemistry, Technion-Israel Institute of Technology, Technion City, Haifa 32000, Israel

^c Shenzhen Institute of Advanced Technology, Chinese Academy of Sciences, Shenzhen 518055, Guangdong, China

^d School of Chemical Engineering, Northwest University, Xi'an, China 710069

^e School of Materials Science and Engineering, Nanyang Technological University, 50 Nanyang Avenue, Singapore 639798, Singapore

^f School of Computational Science and Electronics, Hunan Institute of Engineering, Xiangtan 411104, China

^g Guangdong Provincial Key Lab of Nano-Micro Material Research, School of Chemical Biology and Biotechnology, Peking University Shenzhen Graduate School, Shenzhen 518055, China

ARTICLE INFO

Keywords:

Coherent interface

Heteroepitaxial growth

Nanohybrid

Photochemical conversion

Transition metal chalcogenides

ABSTRACT

Creating atomically coherent interfaces can sharpen the physiochemical properties and functionalities of nanomaterials for efficient energy conversion via manipulating the charge flow. While coherent interfaces can be built between transition metal dichalcogenides with structural similarities and weak interlayer van der Waals interactions, it remains challenging to realize interfacial coherency with more generic transition metal chalcogenides via cost-effective wet chemical routes. Here we establish a coherent CdS(010)|CoS(010) interface via in-situ heteroepitaxial growth of CoS nanoflakes onto CdS nanowires. The uniform and oriented distribution of CoS nanoflakes on the CdS nanowires features an interesting “leaves-on-a-branch” nano-architecture with coherent interface and well-aligned energy levels, allowing efficient separation of photoexcited charge carriers. Combined with the outstanding proton reduction kinetics of the CoS “nanoleaves”, striking photochemical solar-to-hydrogen conversion performance can be obtained. Our findings provide a viable design strategy of nano-junctions with atomic level coherency and great application prospect in catalysis, nanoelectronics and many others.

1. Introduction

Interface engineering of materials at the atomic level via modulation of chemical compositions, crystallographic phases, lattice defects, crystal facets, dopant atoms, etc., has proved viable for generating elaborate nanoarchitectures [1–4]. The abrupt structural and compositional transition in such fine interfacial segments often induces desirable physiochemical properties and functionalities unseen in bulk crystals [5], which could underlie widespread applications in photovoltaics [6], energy conversion [7,8], nanophotonics [9], sensors [10], catalysis activation [11], scatterings [12], nanoelectronics [13], etc. In particular, a coherent interface is formed when two different but facet-matched crystals are conjoined with minimal lattice distortion and

disorder. Such a feature of lattice continuity across the interface [14] is critically important for quantum technologies, such as charge flow control in photoelectronic devices [15–17]. A notable example is the atomically thin interlayer or lateral coherent interface between 2D transition metal chalcogenides (TMCs) constructed via advanced synthetic techniques such as chemical vapor deposition (CVD) [18–20], which opens up a new vista for quantum device concepts impossible with other conventional material constructs.

TMCs, a huge group of promising materials with versatile crystal and electronic structures, have presently attracted tremendous attention in topical fields such as renewable energy conversion and storage [21–23], solar cells [24], catalysis [25], and photodetectors [26]. In sunlight harvesting devices, the local interaction near the grain boundary can

* Corresponding authors.

E-mail addresses: lilac@technion.ac.il (L. Amirav), chsyang@pku.edu.cn (S. Yang), xingzh7@mail.sysu.edu.cn (Z. Xing).

¹ Equally contributed to this work.

largely affect the interfacial electron distribution and charge transfer rate, and thus it is of great interest to exploit interface engineering for promoting the solar energy conversion performance of TMCs [27,28]. For instance, the semiconducting TMC CdS, due to its strong visible light absorption and suitable electronic band positions, has been the research hotspot over the years in the field of photochemical conversions, especially on the construction of heterostructured photocatalysts [29–31]. However, it remains a great challenge to rationally design and grow atomically coherent interfaces between TMCs, except for the van der Waals layered transition metal dichalcogenides (TMDs), via facile wet chemical strategies [32–35].

Herein we report on our success in building a coherent interface between CdS semiconducting nanowires (NWs) and CoS “nanoleaves (NLs)” via a simple hydrothermal route, and in further demonstrating the superior photochemical hydrogen production performance of the nanoarchitecture thus obtained. Importantly, the high percentage of exposed (010) facet of the as-synthesized CdS NWs allows the uniform growth of CoS NLs preferentially in their (010) crystal orientation along the NW perimeter via a tight -Cd-S-Co- bonding switch at the hetero-epitaxial interface, forming CoS-on-CdS branch-like NWs (Cd-Co-S CINWs). The introduction of CoS NLs not only brings about a unique coherently interfaced junction, which minimizes the barrier for charge transfer across the interface and consequently enhances spatial charge separation substantially, but also markedly reduces the surface reaction energy barrier at the exposed CoS (010) facets for proton reduction.

2. Experimental section

Synthesis of CdS Nanowires. In a typical process, 125 mg of Cd ($(\text{CH}_3\text{COO})_2 \cdot 2 \text{H}_2\text{O}$) and 300 mg of thioacetamide were added into 20 mL of ethylenediamine (EDA). After stirring for 1 h to completely dissolve, the mixture was placed in 100 mL of a Teflon-lined autoclave and heated at 180 °C for 16 h, and then the product was collected after cooling to room temperature naturally.

2.1. Synthesis of Hexagonal $\text{Co}(\text{OH})_2$ Nanosheets

The hexagonal $\text{Co}(\text{OH})_2$ nanosheets (NSs) were synthesized according to the literature with some modifications [36]. Briefly, 1 L of 13.3 mM $\text{CoCl}_2 \cdot 2 \text{H}_2\text{O}$ solution and 1 L of 26.7 mM ethanolamine solution were purged by argon for 30 min under stirring, respectively. After that, the ethanolamine solution was injected into the $\text{CoCl}_2 \cdot 2 \text{H}_2\text{O}$ solution slowly under stirring and argon stream. Subsequently, the mixture was purged for another 3 h and then sealed. After purging, the mixture was allowed to react for 36 h under ambient atmospheric condition. Finally, the green products were collected and washed with distilled water three times.

2.2. Synthesis of branch-like Cd-Co-S CINWs

For the synthesis of Cd-Co-S CINWs, 300 μL of the above CdS solution ($\sim 1 \text{ mg}$) without washing was centrifuged and then dissolved in 10 mL of H_2O . Then, 0.8 mg of $\text{Co}(\text{OH})_2$ and 0.65 mg of thiourea were added into the CdS aqueous solution and subjected to ultrasonic dispersion for 30 min. Subsequently, the mixture was transferred to a Teflon-lined autoclave and heated at 180 °C for 14 h. The products were then collected and washed with DI water for three times. Similarly, pure CoS NLs were prepared by the same procedure without CdS addition.

2.3. Synthesis of Cd-Co-S CINWs with different amounts of CoS and impregnated CdS-CoS mixture

The Cd-Co-S CINWs with different amounts of CoS can be synthesized with the same synthesis procedure by using 0.4, 0.6, 0.8, and 1.6 mg of $\text{Co}(\text{OH})_2$ NSs as the precursor and 0.16, 0.33, 0.65, and 1.3 mg of thiourea as S source, respectively, which corresponding to Cd-Co-S

CINWs-0.4, Cd-Co-S CINWs-0.6, Cd-Co-S CINWs-0.8, and Cd-Co-S CINWs-1.6, respectively. As a comparison, a physical mixture of CdS and CoS was prepared via the impregnation method (CdS-CoS(im)). 5.6 mg CdS NWs and 4.4 mg CoS NLs were dispersed in 10 mL of H_2O and then kept at 60 °C for 30 h in an oil bath under stirring. Finally, the CdS-CoS(im) products (with identical CdS/CoS ratio to that of Cd-Co-S CINWs-0.8) were collected by centrifuge and vacuum drying.

2.4. Materials characterization

X-ray powder diffraction (XRD) was carried out by using Rigaku SmartLab 9 kW high-resolution diffraction system. Transmission Electron Microscopy (TEM) and Electron Dispersive Spectroscopy (EDS) were obtained by an FEI Tecnai G² T20 S-Twin TEM, running at 200 keV with a LaB6 electron source and an FEI Titan 80–300KeV S/TEM with High Angle Annular Dark Field Scanning Transmission Electron Microscopy (HAADF-STEM) mode. SEM micrographs were obtained using a Zeiss Ultra-Plus HRSEM. UV-Vis absorption spectroscopy was taken using an Agilent Cary 5000 UV-Vis-NIR spectrophotometer. Photoluminescence (PL) measurements were done using a Fluorolog-3 Fluorometer at room temperature, using standard 10 mm fluorometer cuvettes. X-Ray Photoelectron Spectroscopy (XPS) measurements were performed in an analysis chamber using a Versaprobe III - PHI Instrument (PHI, USA). The core-level binding energies of the different peaks were normalized by setting the binding energy for the C1s at 284.8 eV. The surface potentials of samples were evaluated using Kelvin probe force microscopy (KPFM) and performed on an Asylum Research Cypher-S atomic force microscopy. To prepare for KPFM measurements, the samples were dispersed in deionized water and then spin-coated on a Si substrate. Conductive AC240-TM probes ($\sim 2 \text{ N/m}$, $\sim 70 \text{ kHz}$) were used for all samples. A white light with an intensity of 40 mW/cm^2 was placed next to the sample holder for in-situ measurements.

2.5. Photocatalytic hydrogen production tests

The photocatalytic water splitting was conducted in a custom-built gas-tight reaction cell connected to a 10 mL/min argon line (99.999% purity, filtered through a Triple Filter from Scientific Glass Technology-SGT-F0301) and an Agilent 7890 A Series gas chromatograph with a thermal conductivity detector (GC-TCD). 1 mg of catalyst was dispersed into 10 mL of DI water containing 20% lactic acid, and then the suspension was stirred and purged with argon for 30 min. The samples were then illuminated with a 405 nm LED adjusted to 150 mW (equivalent to a photon flux of 3.06×10^{17} photons/sec). The evolving gas was analyzed by an online gas chromatograph with a 5 Å molecular sieve column. Operation in continuous flow mode allowed for direct determination of the gas production rate. The apparent quantum efficiencies (AQE) of samples are calculated according to the equation: $\text{AQE} = 2N_{\text{H}_2}/N_{\text{hv}}$, where N_{H_2} and N_{hv} are the number of hydrogen molecules produced and the number of incident photons, respectively.

2.6. Photoelectrochemical measurements

Photocurrent tests were performed using an electrochemical workstation (SP-300, Bio-Logic SAS, France) in a standard three-electrode configuration with 0.5 M of Na_2SO_4 as the electrolyte solution. The working, reference, and counter electrodes were the sample, Ag/AgCl, and platinum foil, respectively. The working electrode was prepared as follows: 2.5 mg of as-prepared products were first dispersed into mixtures of DI water (350 μL), and 20 μL of Nafion and sonicating for 60 min to form a homogeneous suspension. Then, 30 μL suspension was dropped onto a pretreated Fluorine doped Tin Oxide (FTO) conductor glass substrate and dried for 8 h at 90 °C under N_2 gas condition with a mass loading of about 0.2 mg/cm^2 . The transient photocurrent was measured with the lamp on and off at a fixed interval of 30 s

All potentials were converted to a reversible hydrogen electrode

(RHE) using the equation: $E_{\text{RHE}} = E_{\text{Ag/AgCl}} + 0.1976 + 0.059 \text{ pH}$. Linear sweep voltammetry (LSV) was performed at a scan rate of $50 \text{ mV} \cdot \text{s}^{-1}$. Tafel plots were presented via replotting polarization curves as over-potential (η) vs. log current ($\log J$) according to the Tafel equation ($\eta = b \cdot \log(J) + a$). Electrochemical impedance spectroscopy (EIS) was measured in the frequency range of 100 kHz to 0.01 Hz applying an AC voltage amplitude of 5 mV. Mott-Schottky (M-S) plots were determined by using a frequency of 1.0 kHz and an amplitude of 5 mV for evaluating the flat band potential of the semiconductor [37].

2.7. Theoretical calculations

The CASTEP module of the Materials Studio software (Accelrys Inc.) was employed for the Density Functional Theory (DFT) calculations. Bulk CoS ($a=b=3.35 \text{ \AA}$, $c=5.14 \text{ \AA}$, $\alpha = \beta = 90^\circ$, $\gamma = 120^\circ$) and CdS ($a=b=4.14 \text{ \AA}$, $c=6.71 \text{ \AA}$, $\alpha = \beta = 90^\circ$, $\gamma = 120^\circ$) were used based on the XRD data. The CoS (010) and CdS (010) facets were chosen since they are two of the most stable facets under practical conditions. The 5×1 supercell of CoS (010) with lattice length $20.555 \text{ \AA} \times 6.693 \text{ \AA}$ was used to match with the 4×2 supercell of CdS (010) with lattice length $20.68 \text{ \AA} \times 6.713 \text{ \AA}$, where the maximum lattice mismatch of the above two surfaces are only 0.61% based on the equation [38]: $\delta = \frac{a-b}{b} \times 100\%$, where δ , a , b are the lattice mismatch, lattice parameters of CdS and CoS, respectively.

During the calculations, self-consistent periodic DFT calculations

were performed with the Tkatchenko-Scheffler method to assess the role of long-range dispersion interactions. The Generalized Gradient Approximation method, in the form of the Perdew-Burke-Ernzerhof approximation, was used to calculate the exchange-correlation energy. The Broyden-Fletcher-Goldfarb-Shanno scheme was chosen as the minimization algorithm. Ionic cores were represented by an ultrasoft pseudopotential. The k-space sampling points were chosen to be $3 \times 4 \times 1$, $3 \times 2 \times 1$, and $1 \times 2 \times 1$ for CoS (010), CdS (010), and CoS (010)/CdS (010) interface. The bottom four layers were fixed to simulate the bulk property. The energy cutoff is 400 eV and the SCF tolerance is $1.0 \times 10^{-6} \text{ eV/atom}$. The optimization ends when the energy, maximum force, maximum stress, and maximum displacement are smaller than $5.0 \times 10^{-6} \text{ eV/atom}$, 0.01 eV/\AA , 0.02 GPa , and $5.0 \times 10^{-4} \text{ \AA}$, respectively.

The free energy of the adsorption atomic hydrogen is obtained according to the equation: $\Delta G_{\text{H}} = \Delta E_{\text{H}} + \Delta E_{\text{ZPE}} - T\Delta S_{\text{H}}$, where ΔG_{H} is the Gibbs free energy, ΔE_{ZPE} denotes the zero-point energy of the system (simplified as 0.05 eV), $-T\Delta S_{\text{H}}$ represents the contribution from entropy at temperature K (0.20 eV at 298 K) [39], describes the energy needed to increase the coverage by one hydrogen atom. ΔE_{H} is calculated according to the equation: $\Delta E_{\text{H}} = E[\text{*} + \text{H}] - E[\text{*}] - 1/2 E[\text{H}_2]$, where $E[\text{*} + \text{H}]$ is the total energy of the system, including the adsorbed molecules and the facets; $E[\text{*}]$ is the energy of facets; $E(\text{H}_2)$ represents the total energy of a gas phase H_2 molecule.

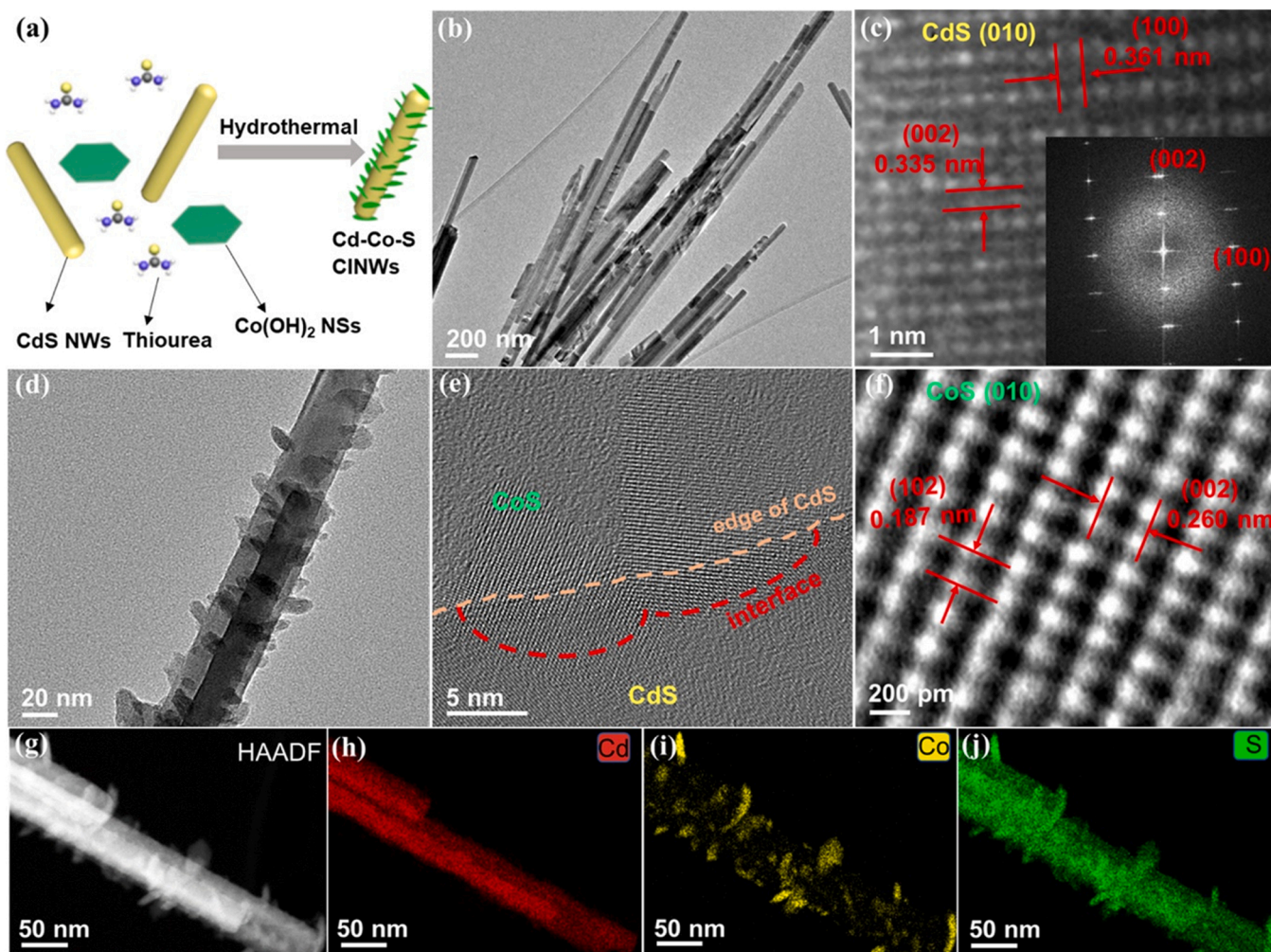


Fig. 1. (a) Schematic illustration of the synthesis of Cd-Co-S CINWs. (b) TEM and (c) HRTEM images of pure CdS NWs. Inset: corresponding FFT pattern. (d) TEM and (e) HRTEM images of Cd-Co-S CINWs. (f) atomic resolution HRTEM image of the CoS area of Cd-Co-S CINWs taken from (e). (g) HAADF-STEM image and (h-j) corresponding elemental maps of typical Cd-Co-S CINWs.

3. Results and discussion

3.1. Formation of the coherent interface between transition metal sulfides

The branch-like Cd-Co-S CINWs were fabricated via a facile wet chemical route, in which the sulfidation of hexagonal $\text{Co}(\text{OH})_2$ nano-sheets (NSs) to CoS NLs and their in-situ epitaxial growth onto the CdS NWs occurred simultaneously (Fig. 1a) [40]. Pure CdS NWs with an average diameter of ca. 50 nm and a length of several hundred nm (Fig. 1b) were first prepared via a solvothermal reaction. In the X-ray diffraction (XRD) pattern (Fig. 2a), all peaks can be well indexed to a wurtzite CdS phase (JCPDS No. 77–2306, hexagonal, $a=b=4.14$ Å, $c=6.71$ Å). Clear lattice fringes of 0.335 and 0.361 nm, which are assigned to the (002) and (100) atomic planes, respectively, are observed in the high-resolution transmission electron microscopy (HRTEM) image (Fig. 1c) [41]. The corresponding fast Fourier transform (FFT) pattern (inset of Fig. 1c) features diffraction spots of the [010] zone, indicating the exposing of (010) facet along the perimeter of CdS NWs [36]. Hexagonal $\beta\text{-Co}(\text{OH})_2$ NSs (JCPDS No. 74–1057) with diameters of 200–300 nm (Fig. S1) were chosen as the precursor to realize the in-situ heteroepitaxial growth of CoS onto the CdS NWs in the presence of thiourea during the hydrothermal reaction. As can be seen from the TEM and scanning electron microscopy (SEM) images of the as-obtained Cd-Co-S CINWs (Fig. 1d, S2d-f), minute flakes (10–20 nm) were uniformly grown onto the CdS NWs, forming an interesting “leaves-on-a-branch” morphology. The XRD results not only demonstrate the wurtzite CdS crystal structure being preserved in Cd-Co-S CINWs, as reflected by the non-shifted peaks, but also confirm the introduction of hexagonal phase CoS (JCPDS No. 65–8977) (Fig. 2a). Elemental maps (Fig. 1g-j) collected with high-angle annular dark-field (HAADF) scanning TEM-energy-dispersive X-ray spectroscopy (HAADF-STEM-EDX) suggest that while S is homogeneously distributed throughout the “leaves-on-a-branch” NWs, Co and Cd are exclusively located on the peripheral NLs, and the stem part, respectively. Thus, a

unique “(CoS) leaves-on- (CdS) branch” architecture can be deduced for the as-prepared Cd-Co-S CINWs. Its EDX spectrum also confirms that Cd, S, and Co are the main elements of Cd-Co-S CINWs (Fig. S3). Meanwhile, the average thickness of pure CoS NLs (see Experimental Section for details) is measured to be ca. 7.2 nm (Fig. S4) by atomic force microscopy (AFM).

To elucidate the atomic interfacial structure between the CdS NWs and CoS NLs in Cd-Co-S CINWs, both atomic resolution HRTEM and theoretical calculations were performed. It can be clearly seen from the HRTEM image near the CoS-CdS boundary (Fig. 1e) that the crystal lattices of CoS NLs smoothly transition to those of CdS NWs without any noticeable interruption, establishing a coherent interface between the “leaves” and the “branch”. An enlarged view of the HRTEM image of the CoS NLs area in Cd-Co-S CINWs (Fig. 1f) unveils the presence of (102) and (002) planes with lattice spacings of 0.187 and 0.260 nm, respectively, testifying the (010) growth orientation of CoS NLs onto the CdS (010) facet. The interfacial coherence in the heteroepitaxial CoS(010)|CdS(010) junction is investigated by Density Functional Theory (DFT) calculations (see experimental for details). Judging from the 5×1 supercell of CoS (010) facet with lattice length 20.555 Å \times 6.693 Å to be matched with the 4×2 supercell of CdS (010) facet with lattice length 20.68 Å \times 6.713 Å, the maximum lattice mismatch between two facets is merely 0.61% (the (001) direction of CoS (20.555 Å) and the (100) direction of CdS (20.68 Å)). In addition, an interface distance as short as 2.227 Å is calculated, which brings the system to the lowest total energy (Fig. S5). This is in good agreement with the intimate contact between CdS and CoS observed in HRTEM. Such a well-established heteroepitaxial CoS(010)|CdS(010) interface is illustrated in Fig. 2e.

Since the epitaxial growth of CoS NLs onto the CdS NWs was realized by the sulfidation of hexagonal $\text{Co}(\text{OH})_2$ NSs in this work, we attempted to modulate the density of CoS NLs grown via tuning the amount of Co(OH)₂ NSs precursor in order to disclose the growth process of CoS (Fig. S2a), with the obtained samples named Cd-Co-S CINWs-X (X stands for the amount of Co(OH)₂ NSs). Interestingly, the CoS NLs tend to first

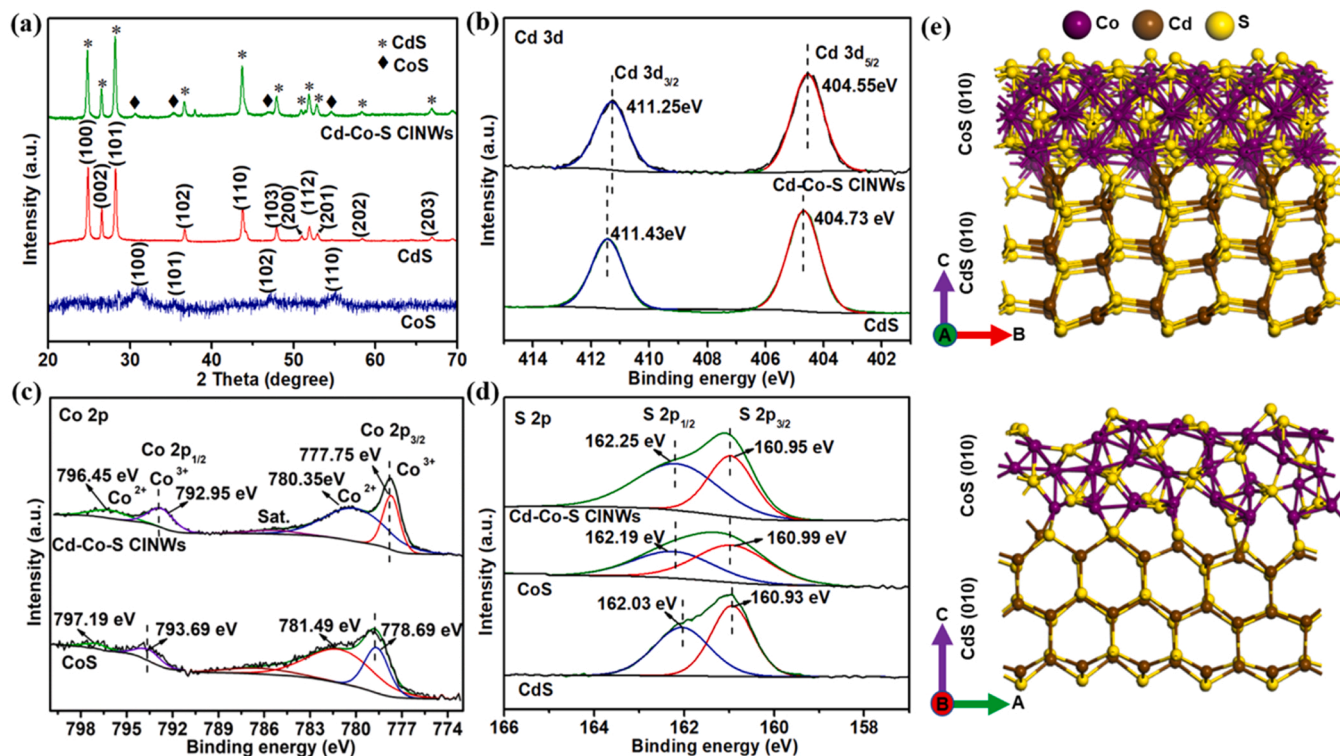


Fig. 2. (a) XRD patterns of pure CoS NLs, CdS NWs and Cd-Co-S CINWs. (b) High-resolution Cd 3d XPS spectra of pure CdS NWs and Cd-Co-S CINWs. (c) High-resolution XPS spectra of Co 2p XPS spectra of pure CoS NLs and Cd-Co-S CINWs. (d) High-resolution S 2p XPS spectra of pure CdS NWs, pure CoS NLs, and Cd-Co-S CINWs. (e) Crystal structure representation of the coherent CdS-CoS interface in Cd-Co-S CINWs with atomic annotation.

grow on the very tip of CdS NWs (Cd-Co-S CINWs-0.4, Fig. S2b&c), when only a small amount of $\text{Co}(\text{OH})_2$ precursor is present, possibly owing to the greater surface energy at the tips than that along the stem of CdS [40, 42, 43]. As the amount of $\text{Co}(\text{OH})_2$ increases, CoS NLs gradually start to grow along the stem surface of CdS NWs (Cd-Co-S CINWs-0.8, Fig. S2d-f), and eventually cover the whole surface of CdS NWs (Cd-Co-S CINWs-1.6, Fig. S2g-i). For simplicity, “Cd-Co-S CINWs” is hereafter referred to as Cd-Co-S CINWs-0.8, which possesses a medium amount of CoS NLs and is used throughout this manuscript if not specified otherwise. It is worth noting that with other Co salt precursors such as CoCl_2 , we were not able to grow any CoS NLs onto the CdS NWs (Fig. S6a), indicating that $\text{Co}(\text{OH})_2$ NSs play an essential role of template during the growth of CoS NLs.

3.2. Structural characterizations of the Cd-Co-S CINWs

The chemical compositions of CdS NWs, Cd-Co-S CINWs and pure CoS were studied with X-ray photoelectron spectroscopy (XPS). The XPS survey spectrum of Cd-Co-S CINWs (Fig. S7) shows the coexistence of Cd, S, and Co elements, further confirming the successful growth of CoS NLs on CdS NWs. As shown in Fig. 2b, the Cd $3d_{5/2}$ and Cd $3d_{3/2}$ doublet peaks at 404.73 and 411.43 eV, respectively, in the high-resolution Cd 3d spectrum of pure CdS NWs slightly shift towards lower binding energy regions (404.55 and 411.25 eV, respectively) upon the introduction of CoS, suggesting the interfacial electronic interaction between CdS and CoS via -Cd-S-Co- bonding [44, 45]. The high-resolution Co 2p spectrum of Cd-Co-S CINWs (Fig. 2c) exhibits doublet peaks of both Co^{3+} (777.75 and 792.95 eV assigned to Co $2p_{3/2}$ and Co $2p_{1/2}$, respectively) and Co^{2+} (780.35 and 796.45 eV of Co $2p_{3/2}$ and Co $2p_{1/2}$, respectively), as well as a satellite peak (Sat.) of Co $2p_{3/2}$ at 785.65 eV [44, 46, 47], which are all negatively shifted compared to the peaks of pure CoS (778.69, 793.69, 781.49, 797.19 and 786.89 eV, respectively), further illustrating the tight bonding between CdS and CoS, which builds a “bridge” for the charge transfer between them [48]. In addition, the S 2p peaks of Cd-Co-S CINWs (160.95 and 162.25 eV corresponding to S $2p_{3/2}$ and S

$2p_{1/2}$, respectively) are located at more positive values than those of CdS (160.93 and 162.03 eV) are (Fig. 2d). Therefore, all the aforementioned XRD, microscopy and XPS analyses verify the establishment of a coherent CdS(010)|CoS(010) interface in the as-prepared Cd-Co-S CINWs.

3.3. Photochemical and photoelectrochemical conversions

The energy conversion capabilities of the as-prepared products are demonstrated with photochemical water reduction to clean hydrogen fuels since CdS is a well-known photocatalyst. A physical mixture of CdS and CoS was synthesized via impregnation (see Experimental Section for details) as a control (CdS-CoS(im)), in which there is a lack of lattice matching (Fig. S6b). Fig. 3a compares the average H_2 evolution rates of pure CdS NWs, CoS NLs, CdS-Pt, CdS-CoS (im) and Cd-Co-S CINWs (including the control samples with different loading amounts of CoS) under LED illumination at 405 nm (150 mW) in the presence of lactic acid as the hole scavenger. Whereas CoS NLs did not produce any appreciable H_2 and pure CdS NWs exhibited a relatively low H_2 generation rate ($2.39 \text{ mmol} \cdot \text{g}^{-1} \cdot \text{h}^{-1}$) due to charge recombination and low surface catalytic activity [49], the heteroepitaxially grown CoS NLs on CdS NWs remarkably enhanced the photochemical HER activity. The best performer, Cd-Co-S CINWs-0.8, can produce H_2 gas at a rate of, astonishingly, $51.94 \text{ mmol} \cdot \text{g}^{-1} \cdot \text{h}^{-1}$, ca. 22 times that of pure CdS NWs (Fig. 3a), and a total amount of $642 \text{ mmol} \cdot \text{g}^{-1}$ of H_2 was accumulated after 12 h of reaction (Fig. 3b). What's more, it is noteworthy that although with identical CdS/CoS ratio to that of Cd-Co-S CINWs-0.8, the CdS-CoS (im) exhibits a much lower hydrogen evolution rate of $14.30 \text{ mmol} \cdot \text{g}^{-1} \cdot \text{h}^{-1}$, clearly highlighting the pivotal role of the coherent interface. However, excessive growth of CoS causes severe photochemical activity deterioration (Cd-Co-S CINWs-1.6), which may result from the reduced light absorption of CdS NWs due to the shading effect of high-density CoS NLs [50]. Furthermore, the apparent quantum efficiencies (AQE) of all samples were calculated based on the incident photon flux and the number of evolved H_2 molecules. In contrast to the

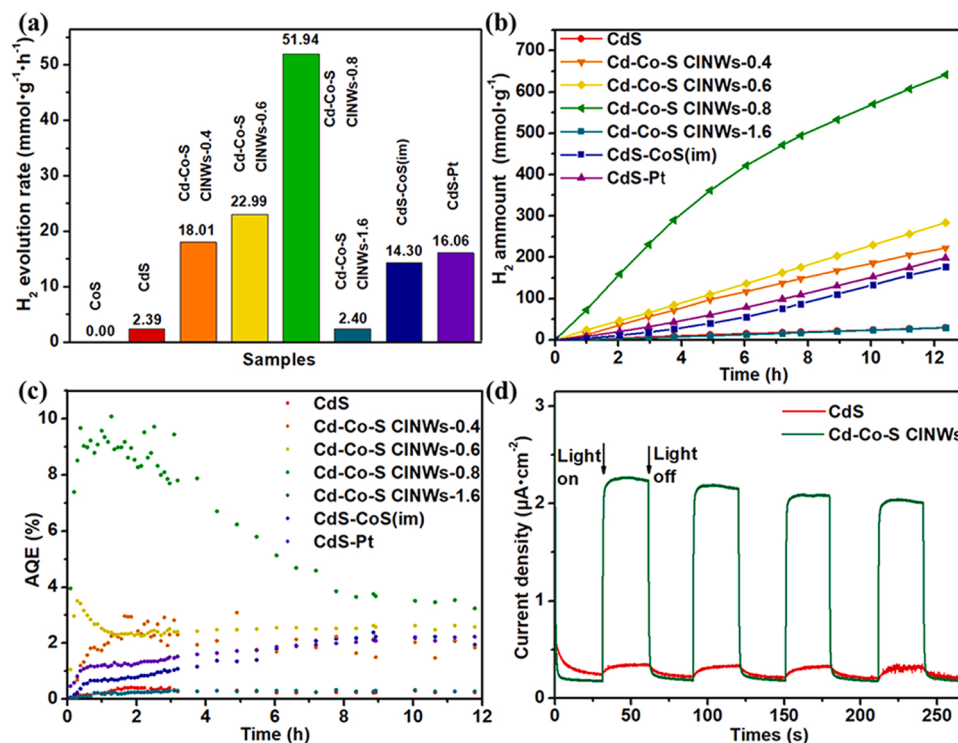


Fig. 3. Comparison of (a) average photocatalytic H_2 evolution rates, (b) H_2 generation time profiles and (c) AQEs of pure CdS, CdS-Pt, CoS, CdS-CoS (im) and Cd-Co-S CINWs with different loading amounts of CoS. (d) Photocurrent versus time measured under chopped illumination at 0.7 V vs Ag/AgCl.

low AQE of only $\sim 0.4\%$ for pure CdS, the AQE of Cd-Co-S CINWs-0.8 ramped up to $\sim 10\%$ within the first 2 h (Fig. 3c), which, barring the gradual decrease with time (likely due to the photocorrosion of CdS), remains higher than that of pure CdS even after 24 h illumination (Fig. S9a). As shown in Fig. S8, a certain degree of photocorrosion occurred for the Cd-Co-S CINWs-0.8 after hydrogen evolution test (surface degradation as observed in the TEM image and slightly weakened XRD peaks), as a result of insufficient supply of sacrificial agents after prolonged illumination. The performance of CINWs has been compared with that of other CdS-based heterostructures, as summarized in Table S1, which highlights the impressive performance of the unique nanostructure in this work. The photoelectrochemical (PEC) response is also tested with photoelectrodes prepared with fresh samples via drop-casting. As shown in Fig. 3d and S9b, Cd-Co-S CINWs produces significantly higher anodic photocurrent densities (over 7 times at 0.7 V vs Ag/AgCl, even higher at other potentials) than CdS does. Since CoS has been proven to be an inactive photocatalyst on its own, the drastically enhanced photochemical and PEC energy conversion efficiencies of Cd-Co-S CINWs strongly indicate the great importance of the specially made coherent interface in conjunction with the CoS NLs with superb properties of charge separation and surface catalysis, respectively.

3.4. Directional charge transport at the CdS-CoS coherent interface

The significantly improved photochemical conversion efficiency of Cd-Co-S CINWs achieved by the atomically coherent interface naturally inspires us to investigate the directional charge transfer across the interface. As shown in Fig. 4a, a strong photoluminescence (PL) emission peak of pure CdS NWs is observed due to the only available channel of radiative recombination, but is remarkably quenched upon the establishment of the heteroepitaxial CdS-CoS junction, thanks to the remarkably promoted charge separation to forestall the radiative

recombination [51]. The visualization of enhanced charge separation has been achieved via monitoring the surface potential change upon light illumination with in-situ Kelvin-probe force microscopy (KPFM) measurements. KPFM directly detects the contact potential difference (CPD) between the scanning tip and the surface of the specimen [52], and the change in CPD reflects charge accumulation or depletion in certain regions. As shown in Fig. 5a-d, the average CPD of pure CdS NWs shifts negatively by 53.1 mV (from -100.4 to -153.5 mV) when irradiated. The epitaxial growth of CoS NLs not only causes a change in the intrinsic CPD value (625.8 mV) in the dark, as a result of the different work function of CoS, but more importantly, induces a much larger negative CPD shift of 128.1 mV upon illumination, which clearly signals the improved charge separation arising from the coherent interface. In theory, the CPD of samples should gradually relax to the original level after the illumination is switched off, and thus the CPD values measured immediately afterwards demonstrate the sample's capability of retaining photoexcited charges. After switching off the illumination, the CPD of pure CdS NWs shifts positively by 15.9 mV, which is up to ca. 30% of the original negative shift. By contrast, the immediate positive shift of Cd-Co-S CINWs after illumination-off (25.9 mV) is only ca. 20% of the original light-induced negative shift, further proving the promoted charge separation at the coherent interface.

To elucidate the charge transfer direction, the charge redistribution at the coherent interface was analyzed in terms of Mulliken charge population and electron density difference map via DFT simulations. As shown in Fig. 4d, there is a Mulliken charge distribution gradient of Cd sites at the CdS side, that is, the positive charges of Cd sites gradually become smaller from the -Cd-S-Co- bridge (0.65–0.70) away from the interface (0.60–0.62 at the 2nd Cd layer, ca. 0.47–0.48 at the 3rd Cd layer). Such a charge gradient will drive the photoexcited electrons to flow from the bulk of CdS to the interface [53,54]. Similarly, there is also a charge gradient of Co sites at the CoS side, with more positive charges

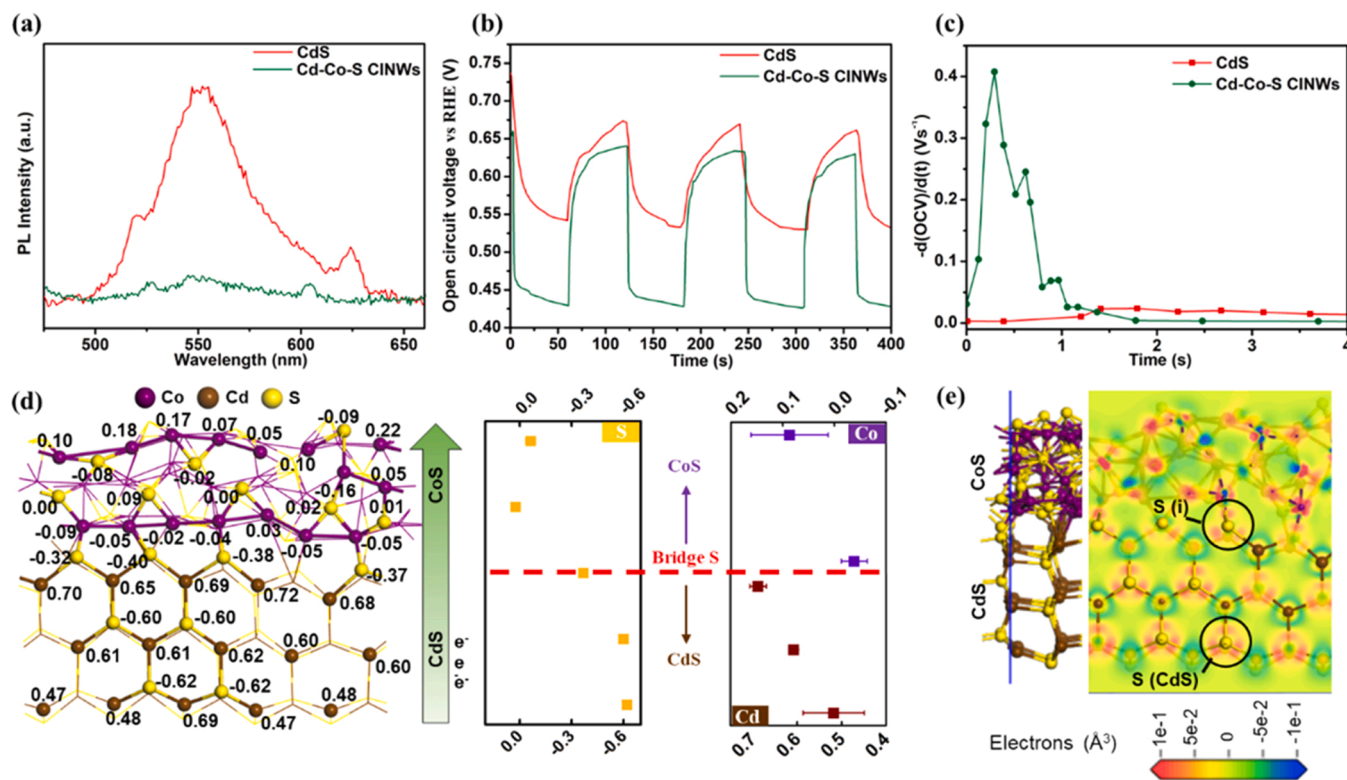


Fig. 4. (a) PL spectra, (b) OCV response to light on/off and (c) Plots of the derivative of OCV with respect to time versus time upon light on of CdS and Cd-Co-S CINWs. (d) Mulliken charge distribution at the interface and the plots of corresponding average charge values of individual elements. (e) Structural model of the heteroepitaxial CoS(010)|CdS(010) junction and calculated electron density difference map of the cross-sectional plane marked by the blue line on the structural model. S(i) and S(CdS) represent the S atoms at the heterojunction interface and bulk CdS, respectively.

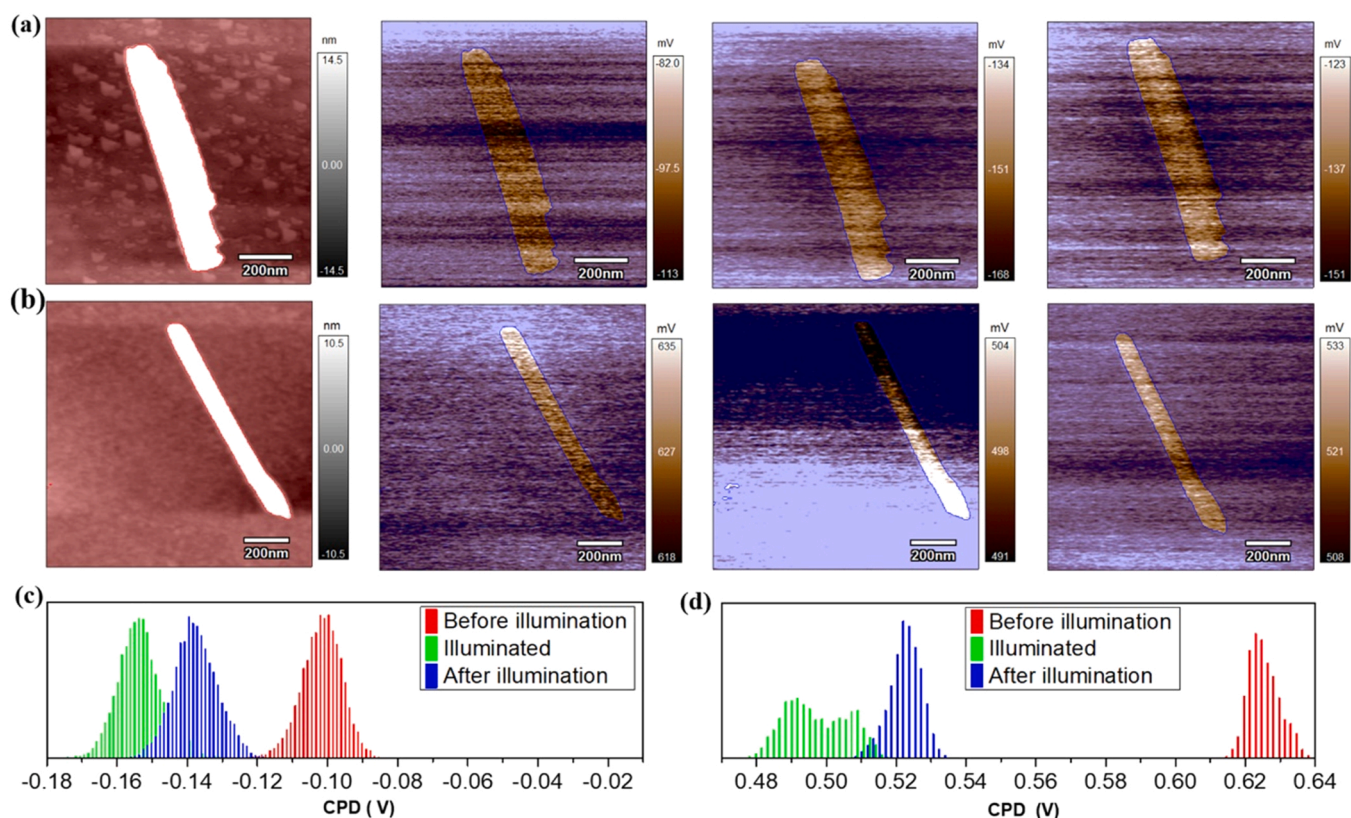


Fig. 5. AFM and KPFM images under different illumination conditions of (a) pure CdS and (b) Cd-Co-S CINWs, respectively. CPD distributions obtained from the sample areas of the KPFM images of (c) pure CdS and (d) Cd-Co-S CINWs, respectively.

away from the -Cd-S-Co- bridge, which facilitates the transport of photoelectrons from the interface towards the bulk of CoS. Interestingly, a continuous Mulliken charge gradient of S sites exists across the interface, with less negative charges from the CdS side to the CoS side. The charge gradients of Cd, Co as well as S can be better visualized with the plots of average charge values of individual elements at different layers (Fig. 4d). Therefore, the charge distribution gradient at both sides of the CdS(010)|CoS(010) interface allows the selective injection of photoelectrons from CdS to CoS, while keeping holes in CdS. In addition, in the calculated electron density difference map (Fig. 4e) with electron-rich and electron-deficient regions marked in red and blue, respectively, one can notice that the electron density around the S atoms at the interface (S (i)) is lower compared to that of the bulk CdS phase (S (CdS)), which favors the photoelectron flow from CdS to CoS at the interface, agreeing well with the Mulliken charge population analysis. The energetics of such directional electron transfer at the coherent CoS (010)|CdS(010) interface will be further verified below.

The separation behavior of photoexcited charge carriers at the semiconductor surface-electrolyte interface was explored by open-circuit photovoltage (OCP) analysis [55–57]. OCP refers to the change of the open circuit voltage (OCV) of a photoelectrode when it is suddenly exposed to illumination [52]. As depicted in Fig. 4b, both the pure CdS NWs and Cd-Co-S CINWs exhibit negative OCP, which is a result of charge separation owing to the formation of a depletion layer at the n-type semiconductor-electrolyte interface [58]. The larger negative OCP of the Cd-Co-S CINWs compared to that of pure CdS NWs suggests that the loading of CoS NLs on CdS NWs can facilitate the surface electron-hole separation [52]. In addition, the derivative of OCV with respect to time was plotted versus time ($-d(OCV)/dt$ vs t) at the initial stage of irradiation (Fig. 4c) and it is discovered that Cd-Co-S CINWs presents a much larger initial $-d(OCV)/dt$ value than pure CdS NWs does before the value goes down to zero (<1.2 s), indicative of more efficient charge separation in the Cd-Co-S CINWs than pure CdS [59]. Fig. 5

3.5. Enhanced water reduction kinetics at the CoS (010) facet

The way how the heteroepitaxial growth of CoS changed the surface HER thermodynamics and kinetics have been studied with electrochemical analysis and DFT calculations. Compared to pure CdS, Cd-Co-S CINWs possesses largely reduced charge-transfer resistance at the semiconductor-electrolyte interface, as reflected by the smaller semi-circle radius in the electrochemical impedance spectroscopy (EIS) Nyquist plots (Fig. 6a) [60]. Linear sweep voltammetry (LSV) curves measured under dark conditions demonstrate the significantly reduced HER overpotential with the introduction of CoS NLs (Fig. 6b), which evidences the much lower thermodynamic energy barrier of HER on the CoS (010) facet compared to that of the CdS (010) facet. In addition, Tafel plots of both pure CdS and Cd-Co-S CINWs (Fig. 6c) are drawn to analyze the kinetics of HER occurring at different locations. Impressively, a substantially lower Tafel slope value of $194 \text{ mV} \cdot \text{dec}^{-1}$ is obtained with Cd-Co-S CINWs than pure CdS NWs ($700 \text{ mV} \cdot \text{dec}^{-1}$), unveiling drastically faster HER kinetics on the CoS (010) facet. To further verify the boosted HER activities of CoS NLs, DFT calculations have been carried out to compare the Gibbs free energy (ΔG_H) on the CdS (010) facet and CoS (010) facet (Fig. 6d). The main descriptor of HER process, that is, the adsorption free energy of the reactive hydrogen intermediate (H^*) [61], is calculated to be smaller for the CoS (010) facet (0.04 eV) than that of the CdS (010) facet (2.49 eV) by a large margin, indicating that the surface of CoS NLs is more catalytically active than the perimeter of CdS NWs towards HER, in good agreement with the electrochemical results.

3.6. Interfacial energetics and mechanism of the photochemical conversions

The interfacial energetics of the as-obtained Cd-Co-S CINWs, which is one of the key factors determining the overall photoconversion

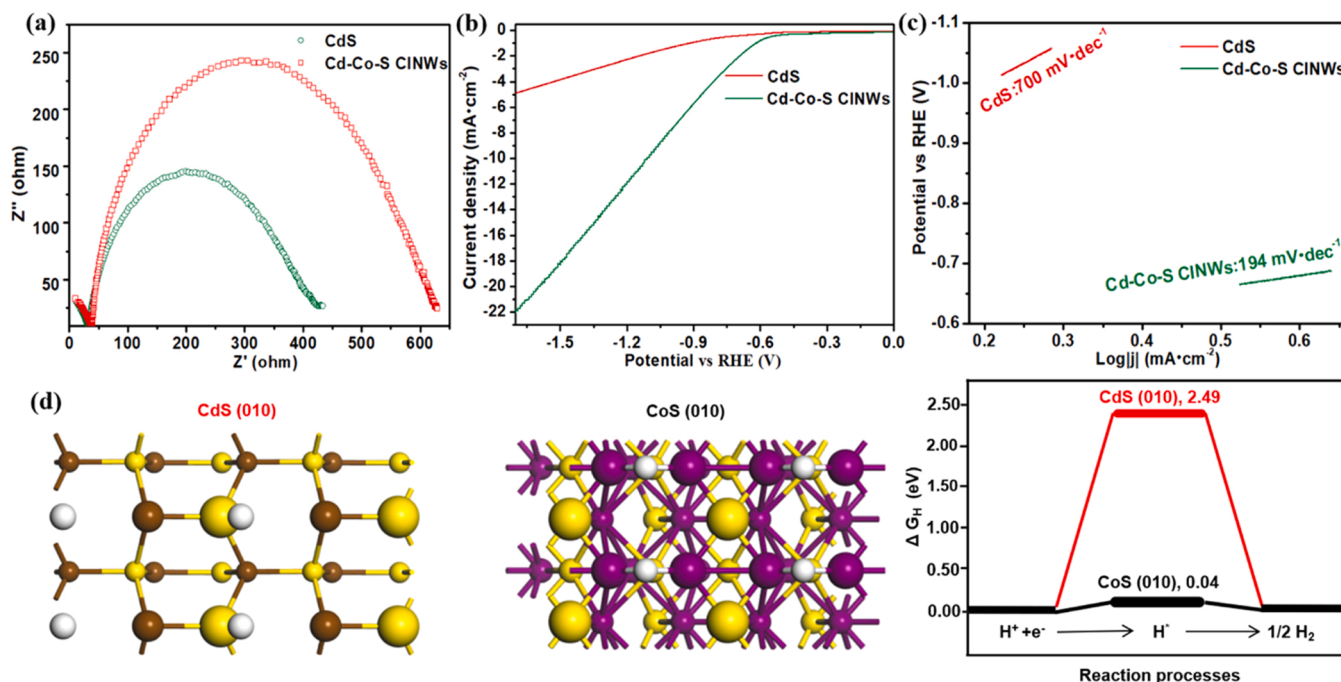


Fig. 6. (a) EIS spectra, (b) Linear sweep voltammetry (LSV) curves measured under dark conditions and (c) Tafel plots of CdS and Cd-Co-S CINWs. (d) Crystal structure models and free energy diagrams for HER based on a single H adatom of the CdS (010) facet and CoS (010) facet.

efficiency, were also investigated. As shown in Fig. 7a, the ultraviolet-visible diffuse reflectance spectra (UV-vis DRS) show that the absorption edge of the yellow CdS NWs is located at 513 nm, whilst the black CoS NLs powder exhibits strong optical absorption in the broad range of 300–800 nm. The heteroepitaxial growth of CoS NLs onto the CdS NWs does not alter the absorption edge of CdS NWs noticeably, but elevates the background beyond the absorption edge owing to the existence of CoS. The band gaps of pure CdS and CoS are calculated to be 2.41 and

0.74 eV, respectively, via the Kubelka-Munk method according to the tangent lines of Tauc plots (Fig. 7b) [62]. In addition, the flat band potentials of CdS and CoS are estimated to be -0.84 and -0.19 V versus NHE, respectively, based on their Mott-Schottky plots (Fig. 7c), which are approximately equal to their conduction band (CB) edges since both CdS and CoS are n-type semiconductors [63,64]. Therefore, based on the band gaps and CB edges of CdS and CoS, the valence band (VB) edges of CdS and CoS are calculated to be 1.57 and 0.55 V versus

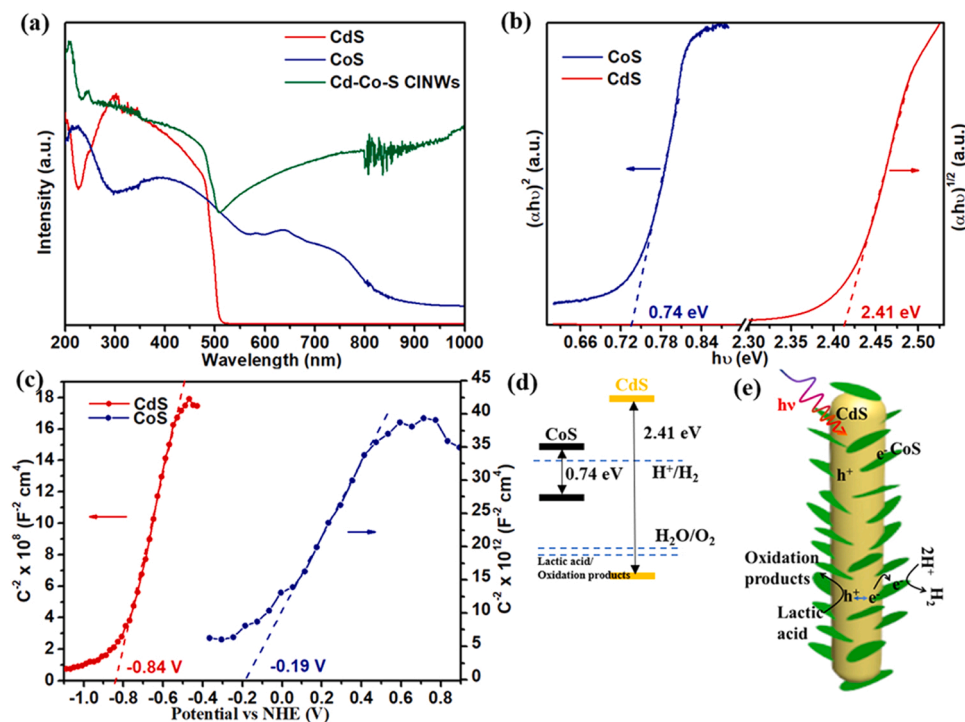


Fig. 7. (a) UV-vis DRS of pure CdS, pure CoS and Cd-Co-S CINWs. (b) Tauc plots and (c) Mott-Schottky plots of pure CdS and pure CoS. (d) Energy level diagram and (e) schematic representation of the proposed photochemical HER mechanism of Cd-Co-S CINWs.

NHE, respectively, which enables us to obtain the energy band alignment of Cd-Co-S CINWs (Fig. 7d). The Fermi level of n-type semiconductor is reported to be located slightly lower than the bottom of CB [65], and thus the CdS NWs possess a higher Fermi level than CoS NLs do, making the electron injection from CdS to CoS an energetically favorable process, in line with the analysis above.

Based on the analysis of electron flow at the atomically coherent CdS (010)-CoS(010) interface and HER performance boost on the CoS (010) facet, a clear mechanism of the photochemical water reduction process can be established. As shown in Fig. 7e, after the CdS NWs are photo-excited and electron-hole pairs produced, the electrons are efficiently injected into the CoS NLs owing to the rationally designed hetero-epitaxial junction, and subsequently protons close to Cd-Co-S CINWs are quickly reduced to H₂ molecules because the CoS (010) facet is highly active for HER. Despite the fact that the band alignment of the CdS-CoS junction resembles a typical straddling gap (type I), which confines both electrons and holes in the small-gap semiconductor, holes are kept in CdS due to the interfacial charge distribution gradient, as verified by PL, KPFM and electrochemical results. When hole scavengers such as lactic acid are present, the holes on CdS will be quickly consumed. Unlike Cd-Co-S CINWs with both well-confined charge transfer channels and abundant HER active sites, pure CdS NWs produce H₂ at a very low rate, and even when loaded with 2 wt% Pt particles, a noble metal benchmark HER catalyst, only exhibits a H₂ production rate (16.06 mmol·g⁻¹·h⁻¹) that is 70% lower than Cd-Co-S CINWs-0.8 does. In addition, the photodeposition of Pt particles onto Cd-Co-S CINWs does not lead to any noticeable HER improvement (Fig. S10), indicating that the CoS NLs are providing adequate active sites for HER.

4. Conclusions

In summary, we have developed a simple wet chemical protocol to fabricate a unique heteroepitaxial junction between CdS nanowires and peripheral CoS nanoflakes (Cd-Co-S CINWs). The highly coherent junction, enabled by the minute lattice mismatch between the (010) facets of both phases, is abrupt with a bridged -Cd-S-Co- bonding switch. The rationally designed nanoarchitecture not only allows the efficient injection of photoexcited electrons from CdS to CoS due to the atomically coherent CdS(010)|CoS(010) interface and the appropriate alignment of energy levels, but also provides much more favorable HER kinetics by exposing the highly active CoS (010) facet, as proved by thorough electrochemical and spectral studies, in-situ KPFM measurements and DFT calculations. As a result, the optimized product exhibits a photochemical H₂ generation rate as high as 51.94 mmol·g⁻¹·h⁻¹, 22-fold higher than that of pure CdS and over 2.6-fold higher than that of the physical CdS-CoS mixture. More importantly, the material design strategy at the atomic level demonstrated in this work opens up new possibilities for cost-efficiently constructing coherent interfaces between various chalcogenides and possibly other materials of key interest in modern photoelectronics.

CRediT authorship contribution statement

Yuxing Chen: Conceptualization, Methodology, Formal analysis, Investigation, Writing – original draft, Writing – review & editing. **Ming Ma:** Methodology, Formal analysis, Resources, Funding acquisition. **Jun Hu:** Methodology, Software, Investigation, Resources, Writing – original draft. **Zhong Chen:** Software, Resources. **Peng Jiang:** Methodology, Investigation. **Lilac Amirav:** Resources, Writing – original draft, Supervision, Funding acquisition. **Shihe Yang:** Conceptualization, Formal analysis, Resources, Writing – original draft, Writing – review & editing, Supervision, Funding acquisition. **Zheng Xing:** Conceptualization, Methodology, Formal analysis, Investigation, Resources, Writing – original draft, Writing – Writing, Supervision, Project administration, Funding acquisition.

Declaration of Competing Interest

The authors declare that they have no known competing financial interests or personal relationships that could have appeared to influence the work reported in this paper.

Data Availability

Data will be made available on request.

Acknowledgments

This work was financially supported by the Guangdong Basic and Applied Basic Research Foundation (2021A151511234), Natural Science Foundation of China (22202237, 21972006, 21676216, 21905298), Shenzhen Science and Technology Innovation Committee (JCYJ20190807164205542), Shenzhen Peacock Plan (KQTD2016053015544057), and Special project of Shaan-xi Provincial Education Department, China (20JC034). Y.C. (202108280008) was funded by the China Scholarship Council (2021).

Appendix A. Supporting information

Supplementary data associated with this article can be found in the online version at doi:10.1016/j.apcatb.2022.122300.

References

- [1] G. Giri, R. Li, D.-M. Smilgies, E.Q. Li, Y. Diao, K.M. Lenn, M. Chiu, D.W. Lin, R. Allen, J. Reinspach, One-dimensional self-confinement promotes polymorph selection in large-area organic semiconductor thin films, *Nat. Commun.* 5 (2014) 1–8.
- [2] F.A. Laskowski, S.Z. Oener, M.R. Nellist, A.M. Gordon, D.C. Bain, J.L. Fehrs, S. W. Boettcher, Nanoscale semiconductor/catalyst interfaces in photoelectrochemistry, *Nat. Mater.* 19 (2020) 69–76.
- [3] V.R. Stamenkovic, D. Strmcnik, P.P. Lopes, N.M. Markovic, Energy and fuels from electrochemical interfaces, *Nat. Mater.* 16 (2017) 57–69.
- [4] N. Reyren, S. Thiel, A. Caviglia, L.F. Kourkouts, G. Hammerl, C. Richter, C. W. Schneider, T. Kopp, A.-S. Rüetschi, D. Jaccard, Superconducting interfaces between insulating oxides, *Science* 317 (2007) 1196–1199.
- [5] N. Shibata, S. Findlay, S. Azuma, T. Mizoguchi, T. Yamamoto, Y. Ikumura, Atomic-scale imaging of individual dopant atoms in a buried interface, *Nat. Mater.* 8 (2009) 654–658.
- [6] M. Graetzel, R.A. Janssen, D.B. Mitzi, E.H. Sargent, Materials interface engineering for solution-processed photovoltaics, *Nature* 488 (2012) 304–312.
- [7] K. Sivula, R. van de Krol, Semiconducting materials for photoelectrochemical energy conversion, *Nat. Rev. Mater.* 1 (2016) 15010.
- [8] F. Lin, S.W. Boettcher, Adaptive semiconductor/electrocatalyst junctions in water-splitting photoanodes, *Nat. Mater.* 13 (2014) 81–86.
- [9] P. Irvin, Y. Ma, D.F. Bogorin, C. Cen, C.W. Bark, C.M. Folkman, C.-B. Eom, J. Levy, Rewritable nanoscale oxide photodetector, *Nat. Photonics* 4 (2010) 849–852.
- [10] G.S. Kulkarni, K. Reddy, Z. Zhong, X. Fan, Graphene nanoelectronic heterodyne sensor for rapid and sensitive vapour detection, *Nat. Commun.* 5 (2014) 1–7.
- [11] Y. Zhang, J. Zhang, B. Zhang, R. Si, B. Han, F. Hong, Y. Niu, L. Sun, L. Li, B. Qiao, Boosting the catalysis of gold by O₂ activation at Au-SiO₂ interface, *Nat. Commun.* 11 (2020) 1–10.
- [12] A.L. Holsteen, S. Raza, P. Fan, P.G. Kik, M.L. Brongersma, Purcell effect for active tuning of light scattering from semiconductor optical antennas, *Science* 358 (2017) 1407–1410.
- [13] N. Strkalj, C. Gattinoni, A. Vogel, M. Campanini, R. Haerdi, A. Rossi, M.D. Rossell, N.A. Spaldin, M. Fiebig, M. Trassin, In-situ monitoring of interface proximity effects in ultrathin ferroelectrics, *Nat. Commun.* 11 (2020) 5815.
- [14] R. Smallman, A. Ngan. Chapter 10-Surfaces, Grain Boundaries and Interfaces, *Modern Physical Metallurgy*, Eighth edition, Butterworth-Heinemann, Oxford, 2014, pp. 415–442.
- [15] M.U. Rothmann, J.S. Kim, J. Borchert, K.B. Lohmann, C.M. O’Leary, A.A. Sheader, L. Clark, H.J. Snaith, M.B. Johnston, P.D. Nellist, L.M. Herz, Atomic-scale microstructure of metal halide perovskite, *Science* 370 (2020) eabb5940.
- [16] S. Gazibegovic, D. Car, H. Zhang, S.C. Balk, J.A. Logan, M.W.A. de Moor, M. C. Cassidy, R. Schmits, D. Xu, G.Z. Wang, P. Krogstrup, R. Veld, K. Zuo, Y. Vos, J. Shen, D. Bouman, B.S. Hojajei, D. Pennachio, J.S. Lee, P.J. van Veldhoven, S. Koelling, M.A. Verheijen, L.P. Kouwenhoven, C.J. Palmstrom, E. Bakkers, Epitaxy of advanced nanowire quantum devices, *Nature* 548 (2017) 434–438.
- [17] Y.H. Zhu, J. Ciston, B. Zheng, X.H. Miao, C. Czarnik, Y.C. Pan, R. Sougrat, Z.P. Lai, C.E. Hsiung, K.X. Yao, I. Pinnau, M. Pan, Y. Han, Unravelling surface and interfacial structures of a metal-organic framework by transmission electron microscopy, *Nat. Mater.* 16 (2017) 532–536.

- [18] J. Xia, J. Yan, Z. Wang, Y. He, Y. Gong, W. Chen, T.C. Sum, Z. Liu, P.M. Ajayan, Z. Shen, Strong coupling and pressure engineering in WSe_2 - MoSe_2 heterobilayers, *Nat. Phys.* 17 (2021) 92–98.
- [19] Y.C. Lin, C.H. Yeh, H.C. Lin, M.D. Siao, Z. Liu, H. Nakajima, T. Okazaki, M.Y. Chou, K. Suenaga, P.W. Chiu, Stable 1T tungsten disulfide monolayer and its junctions: growth and atomic structures, *ACS Nano* 12 (2018) 12080–12088.
- [20] Y.C. Zou, Z.G. Chen, S.J. Liu, K. Aso, C.X. Zhang, F.T. Kong, M. Hong, S. Matsumura, K. Cho, J. Zou, Atomic insights into phase evolution in ternary transition-metal dichalcogenides nanostructures, *Small* 14 (2018), 1800780.
- [21] L. Meng, S. Wang, F. Cao, W. Tian, R. Long, L. Li, Doping-induced amorphization, vacancy, and gradient energy band in SnS_2 nanosheet arrays for improved photoelectrochemical water splitting, *Angew. Chem., Int. Ed.* 58 (2019) 6761–6765.
- [22] M.-R. Gao, J.-X. Liang, Y.-R. Zheng, Y.-F. Xu, J. Jiang, Q. Gao, J. Li, S.-H. Yu, An efficient molybdenum disulfide/cobalt diselenide hybrid catalyst for electrochemical hydrogen generation, *Nat. Commun.* 6 (2015) 1–7.
- [23] M. Chowalla, H.S. Shin, G. Eda, L.-J. Li, K.P. Loh, H. Zhang, The chemistry of two-dimensional layered transition metal dichalcogenide nanosheets, *Nat. Chem.* 5 (2013) 263–275.
- [24] L. Li, N. Coates, D. Moses, Solution-processed inorganic solar cell based on in situ synthesis and film deposition of CuInS_2 nanocrystals, *J. Am. Chem. Soc.* 132 (2010) 22–23.
- [25] X. Wang, X. Wang, J. Huang, S. Li, A. Meng, Z. Li, Interfacial chemical bond and internal electric field modulated Z-scheme $\text{Sv-ZnIn}_2\text{S}_4/\text{MoSe}_2$ photocatalyst for efficient hydrogen evolution, *Nat. Commun.* 12 (2021) 1–11.
- [26] J. Xu, E. Oksenberg, R. Popovitz-Biro, K. Rechav, E. Joselevich, Bottom-up tri-gate transistors and submicrosecond photodetectors from guided CdS nanowalls, *J. Am. Chem. Soc.* 139 (2017) 15958–15967.
- [27] J. Huang, S. He, J.L. Goodsell, J.R. Mulcahy, W. Guo, A. Angerhofer, W.D. Wei, Manipulating atomic structures at the Au/TiO_2 interface for O_2 activation, *J. Am. Chem. Soc.* 142 (2020) 6456–6460.
- [28] X. Hong, J. Kim, S.-F. Shi, Y. Zhang, C. Jin, Y. Sun, S. Tongay, J. Wu, Y. Zhang, F. Wang, Ultrafast charge transfer in atomically thin MoS_2/WS_2 heterostructures, *Nat. Nanotechnol.* 9 (2014) 682–686.
- [29] L. Cheng, Q.J. Xiang, Y.L. Liao, H.W. Zhang, CdS -Based photocatalysts, *Energy Environ. Sci.* 11 (2018) 1362–1391.
- [30] G.N. Liu, C. Kolodziej, R. Jin, S.P. Qi, Y.B. Lou, J.X. Chen, D.C. Jiang, Y.X. Zhao, C. Burda, MoS_2 -stratified $\text{CdS-Cu}_2\text{-S}$ core-shell nanorods for highly efficient photocatalytic hydrogen production, *ACS Nano* 14 (2020) 5468–5479.
- [31] J.X. Low, B.Z. Dai, T. Tong, C.J. Jiang, J.G. Yu, In situ irradiated X-Ray photoelectron spectroscopy investigation on a direct Z-scheme TiO_2/CdS composite film photocatalyst, *Adv. Mater.* 31 (2019), 1802981.
- [32] J. Chen, X.-J. Wu, Y. Gong, Y. Zhu, Z. Yang, B. Li, Q. Lu, Y. Yu, S. Han, Z. Zhang, Edge epitaxy of two-dimensional MoSe_2 and MoS_2 nanosheets on one-dimensional nanowires, *J. Am. Chem. Soc.* 139 (2017) 8653–8660.
- [33] S. Xie, L. Tu, Y. Han, L. Huang, K. Kang, K.U. Lao, P. Poddar, C. Park, D.A. Muller, R.A. DiStasio, Coherent, atomically thin transition-metal dichalcogenide superlattices with engineered strain, *Science* 359 (2018) 1131–1136.
- [34] Y. Liu, J. Li, W. Huang, Y. Zhang, M. Wang, X. Gao, X. Wang, M. Jin, Z. Hou, G. Zhou, Surface-Induced 2D/1D Heterostructured Growth of $\text{ReS}_2/\text{CoS}_2$ for High-Performance Electrocatalysts, *ACS Appl. Mater. Interfaces* 12 (2020) 33586–33594.
- [35] J. Chen, X.J. Wu, Q. Lu, M. Zhao, P.F. Yin, Q. Ma, G.H. Nam, B. Li, B. Chen, H. Zhang, Preparation of $\text{CdS}_x\text{Se}_{1-y}\text{MoS}_2$ heterostructures via cation exchange of pre-epitaxially synthesized $\text{Cu}_{2-x}\text{S}_y\text{Se}_{1-y}\text{MoS}_2$ for photocatalytic hydrogen evolution, *Small* 17 (2021), 2006135.
- [36] S. Gao, Y.F. Sun, F.C. Lei, L. Liang, J.W. Liu, W.T. Bi, B.C. Pan, Y. Xie, Ultrahigh energy density realized by a single-layer $\beta\text{-Co(OH)}_2$ all-solid-state asymmetric supercapacitor, *Angew. Chem. Int. Ed.* 53 (2014) 12789–12793.
- [37] W. Guo, H. Luo, Z. Jiang, D. Fang, J. Chi, W. Shanguan, Z. Wang, L. Wang, A. F. Lee, Ge-doped cobalt oxide for electrocatalytic and photocatalytic water splitting, *ACS Catal.* 12 (2022) 12000–12013.
- [38] F.J. Si, F.L. Tang, H.T. Xue, Electronic properties of NiO (110)/ $\text{CH}_3\text{NH}_3\text{PbI}_3$ (100) interface from the first-principles calculations, *Chem. Phys. Lett.* 707 (2018) 133–139.
- [39] J. Hu, S.L. Zheng, X. Zhao, X. Yao, Z. Chen, A theoretical study on the surface and interfacial properties of Ni_3P for the hydrogen evolution reaction, *J. Mater. Chem. A* 6 (2018) 7827–7834.
- [40] H. Lv, Y. Liu, H. Tang, P. Zhang, J. Wang, Synergetic effect of MoS_2 and graphene as cocatalysts for enhanced photocatalytic activity of BiPO_4 nanoparticles, *Appl. Surf. Sci.* 425 (2017) 100–106.
- [41] Y. Chen, K. Dong, L. Amirav, Ternary dumbbell nanowires for photocatalytic hydrogen production, *Chem. Mater.* 34 (2022) 9373–9383.
- [42] T. Mokari, C.G. Sztrum, A. Salant, E. Rabani, U. Banin, Formation of asymmetric one-sided metal-tipped semiconductor nanocrystal dots and rods, *Nat. Mater.* 4 (2005) 855–863.
- [43] S.E. Habas, P. Yang, T. Mokari, Selective growth of metal and binary metal tips on CdS nanorods, *J. Am. Chem. Soc.* 130 (2008) 3294–3295.
- [44] L. Zhang, L. Feng, P. Li, X. Chen, J. Jiang, S. Zhang, C. Zhang, G. Chen, H. Wang, Direct Z-scheme photocatalyst of hollow CoS_x/CdS polyhedron constructed by ZIF-67-templated one-pot solvothermal route: a signal-on photoelectrochemical sensor for mercury (II), *Chem. Eng. J.* 395 (2020), 125072.
- [45] X.-L. Yin, L.-L. Li, W.-J. Jiang, Y. Zhang, X. Zhang, L.-J. Wan, J.-S. Hu, MoS_2/CdS nanosheets-on-nanorod heterostructure for highly efficient photocatalytic H_2 generation under visible light irradiation, *ACS Appl. Mater. Interfaces* 8 (2016) 15258–15266.
- [46] H. Liang, D. Jiang, S. Wei, X. Cao, T. Chen, B. Huo, Z. Peng, C. Li, J. Liu, 3D cellular $\text{CoS}_{1.097}$ /nitrogen doped graphene foam: a durable and self-supported bifunctional electrode for overall water splitting, *J. Mater. Chem. A* 6 (2018) 16235–16245.
- [47] H. Yuan, J. Liu, H. Li, K. Su, X. Liu, Y. Li, D. Shi, Q. Wu, Y. Zhao, Q. Jiao, Rational integration of hierarchical structural $\text{CoS}_{1.097}$ nanosheets/reduced graphene oxide nanocomposites with enhanced electrocatalytic performance for triiodide reduction, *Carbon* 126 (2018) 514–521.
- [48] B. Qiu, Q. Zhu, M. Du, L. Fan, M. Xing, J. Zhang, Efficient solar light harvesting $\text{CdS}/\text{Co}_3\text{S}_8$ hollow cubes for Z-scheme photocatalytic water splitting, *Angew. Chem., Int. Ed.* 56 (2017) 2684–2688.
- [49] K. Zhang, J. Ran, B. Zhu, H. Ju, J. Yu, L. Song, S.Z. Qiao, Nanoconfined nickel@carbon core-shell cocatalyst promoting highly efficient visible-light photocatalytic H_2 production, *Small* 14 (2018), 1801705.
- [50] Y. Hou, A.B. Laursen, J. Zhang, G. Zhang, Y. Zhu, X. Wang, S. Dahl, I. Chorkendorff, Layered nanojunctions for hydrogen-evolution catalysis, *Angew. Chem., Int. Ed.* 52 (2013) 3621–3625.
- [51] W. Guo, H. Luo, Z. Jiang, W. Shanguan, In-situ pressure-induced $\text{BiVO}_4/\text{Bi}_{0.6}\text{Y}_{0.4}\text{VO}_4$ S-scheme heterojunction for enhanced photocatalytic overall water splitting activity, *Chin. J. Catal.* 43 (2022) 316–328.
- [52] Z. Xing, J. Hu, M. Ma, H. Lin, Y. An, Z. Liu, Y. Zhang, J. Li, S. Yang, From one to two: in situ construction of an ultrathin 2D–2D closely bonded heterojunction from a single-phase monolayer nanosheet, *J. Am. Chem. Soc.* 141 (2019) 19715–19727.
- [53] L.M. Sun, L. Xiang, X. Zhao, C.J. Jia, J. Yang, Z. Jin, X.F. Cheng, W.L. Fan, Enhanced visible-light photocatalytic activity of BiOI/BiOCl heterojunctions: key role of crystal facet combination, *ACS Catal.* 5 (2015) 3540–3551.
- [54] Z. Teng, N. Yang, H. Lv, S. Wang, M. Hu, C. Wang, D. Wang, G. Wang, Edge-functionalized g- C_3N_4 nanosheets as a highly efficient metal-free photocatalyst for safe drinking water, *Chem* 5 (2019) 664–680.
- [55] M. Zhong, T. Hisatomi, Y. Kuang, J. Zhao, M. Liu, A. Iwase, Q. Jia, H. Nishiyama, T. Minegishi, M. Nakabayashi, Surface modification of CoO_x loaded BiVO_4 photoanodes with ultrathin p-type NiO layers for improved solar water oxidation, *J. Am. Chem. Soc.* 137 (2015) 5053–5060.
- [56] S. Bai, L. Yang, C. Wang, Y. Lin, J. Lu, J. Jiang, Y. Xiong, Boosting photocatalytic water splitting: interfacial charge polarization in atomically controlled core-shell cocatalysts, *Angew. Chem. Int. Ed.* 54 (2015) 14810–14814.
- [57] H.-i Kim, D. Monllor-Satoca, W. Kim, W. Choi, N-doped TiO_2 nanotubes coated with a thin TaO_xN_y layer for photoelectrochemical water splitting: dual bulk and surface modification of photoanodes, *Energy Environ. Sci.* 8 (2015) 247–257.
- [58] X. Yue, S. Yi, R. Wang, Z. Zhang, S. Qiu, Well-controlled $\text{SrTiO}_3@ \text{Mo}_2\text{C}$ core-shell nanofiber photocatalyst: boosted photo-generated charge carriers transportation and enhanced catalytic performance for water reduction, *Nano Energy* 47 (2018) 463–473.
- [59] Y.F. Hu, Y.Q. Wu, J.Y. Feng, H.T. Huang, C.C. Zhang, Q.F. Qian, T. Fang, J. Xu, P. Wang, Z.S. Li, Z.G. Zou, Rational design of electrocatalysts for simultaneously promoting bulk charge separation and surface charge transfer in solar water splitting photoelectrodes, *J. Mater. Chem. A* 6 (2018) 2568–2576.
- [60] W. Guo, P. Yu, H. Luo, J. Chi, Z. Jiang, X. Liu, W. Wen, W. Shanguan, Unveiling the role of surface heterostructure in $\text{Bi}_{0.5}\text{Y}_{0.5}\text{VO}_4$ solid solution for photocatalytic overall water splitting, *J. Catal.* 406 (2022) 193–205.
- [61] Y. Jiao, Y. Zheng, M. Jaroniec, S.Z. Qiao, Design of electrocatalysts for oxygen-and hydrogen-involving energy conversion reactions, *Chem. Soc. Rev.* 44 (2015) 2060–2086.
- [62] X. Yue, S. Yi, R. Wang, Z. Zhang, S. Qiu, Cobalt phosphide modified titanium oxide nanophotocatalysts with significantly enhanced photocatalytic hydrogen evolution from water splitting, *Small* 13 (2017), 1603301.
- [63] G. Zhang, D. Chen, N. Li, Q. Xu, H. Li, J. He, J. Lu, Construction of hierarchical hollow $\text{Co}_9\text{S}_8/\text{ZnIn}_2\text{S}_4$ tubular heterostructures for highly efficient solar energy conversion and environmental remediation, *Angew. Chem., Int. Ed.* 132 (2020) 8332–8338.
- [64] S. Wang, B.Y. Guan, Y. Lu, X.W.D. Lou, Formation of hierarchical $\text{In}_2\text{S}_3\text{-CdIn}_2\text{S}_4$ heterostructured nanotubes for efficient and stable visible light CO_2 reduction, *J. Am. Chem. Soc.* 139 (2017) 17305–17308.
- [65] S. Das, S. Patnaik, K. Parida, Dynamic charge transfer through Fermi level equilibration in the p- CuFe_2O_4 /n- NiAl LDH interface towards photocatalytic application, *Catal. Sci. Technol.* 10 (2020) 6285–6298.